
# Drag reduction of ship airflow using steady Coanda effect

Ocean Engineering 266 (2022) 113051

Contents lists available at ScienceDirect

Ocean Engineering

journal homepage: www.elsevier.com/locate/oceaneng

# Drag reduction of ship airflow using steady Coanda effect

Kewei Xu, Xinchao Su, Rickard Bensow, Sinisa Krajnovic *

*Department of Mechanics and Maritime Sciences, Chalmers University of Technology, Gothenburg, 412 96, Sweden*

ARTICLE INFO

*Keywords:*
Ship airflow control
Drag reduction
Coanda effect
Energy efficiency
Large Eddy Simulation (LES)
Experiments

ABSTRACT

This paper studies the steady Coanda effect for reducing the aerodynamic drag of the Chalmers ship model (CSM) using Large Eddy Simulation (LES) with Wall-Adapting Local-Eddy Viscosity (WALE) model. The flow control mechanism is explored, and the analysis of energy efficiency is conducted to evaluate the net benefit of the flow control. Validating the numerical methods, the predicted aerodynamic drag of the ship and pressure coefficients distribution on the baseline CSM agree well with the experimental measurements and the maximum discrepancy is 4.2%. In creating the flow control models, the hanger base of the baseline CSM is modified with a Coanda surface and two different sizes of jet-blowing slots, 1%$h$ (hanger height) and 2%$h$, respectively. A drag reduction of 5.34% is achieved by the 1%$h$ slot-size case. The 2%$h$ slot-size case further increases the drag reduction to 6.22% but has doubled power consumption. It is found that vectoring vorticity towards the low-speed area on deck is effective for enhancing the energization. Finally, the analysis of energy efficiency indicates that the net benefit is achieved in both flow control cases, and the case with the 1%$h$ slot size is 11.9% more efficient due to a stronger Coanda effect.

## 1. Introduction

The ship air wake downstream the superstructure is characterized by large unsteadiness, massive separation, and complex shear layer interactions. It is therefore acquiring increasing attentions and has been studied numerically and experimentally (Syms, 2008; Forrest and Owen, 2010; Herry et al., 2011; Kääriä et al., 2013; Gallas et al., 2017; Crozon et al., 2018). Due to such complicated flow structures, an uncontrolled ship air wake can lead to detrimental effects on helicopter operations, sailing safety, vessel comfort, and power consumption of propulsion. In this regard, various flow control methods have been studied to control or manipulate ship air wake.

Categorizing the flow control methods by the requirement of external flow source, there are passive flow control (PFC) and active flow control (AFC) methods. For PFC methods, certain efforts have been made on optimizing the shape of the hanger. To create the aerodynamically optimized hanger, Bardera et al. (2021b) modified the hanger to a similar shape of the re-circulation bubble. The angled and elliptical hangers with roof and walls modified achieved the best performance in terms of reduction of low-speed area, mitigation of unsteadiness, and loss of interior volume. Bardera and Meseguer (2015) modified the hanger roof of Simple Frigate Shape (SFS) models with different degrees of curvature. It was found experimentally that the "C" shape model with the highest degrees of curvature achieved the maximum reduction of shear layer length by 42%. Furthermore, Shafer and Ghee (2005) achieved a reduction of unsteadiness up to 4.1% by only changing the surface material from solid to porous deck and hanger base.

Shape modification of rounding square to convex shape can possibly induce the Coanda effect which is the tendency of a fluid jet to stay attached to a convex surface (Tritton, 2012). The Coanda effect is therefore constantly used for modifying jet directions. It reduces the pressure on the convex surface by flow entrainment and attaches the jet by the positive pressure gradient pointing from the ambient to the convex surface as shown in Fig. 1. The Coanda effect has been widely used in bluff bodies (Freund and Mungal, 1994; Barros et al., 2016; Haffner et al., 2020) and ground vehicles (Geropp and Odenthal, 2000; Kee et al., 2001) for drag reduction and in airfoils for improving aerodynamic performance (Jones et al., 2002; Sellars et al., 2002; Jones, 2005; Seele et al., 2013).

For the active flow control methods studied on ships, Gallas et al. (2017) implemented steady blowing jet along the hanger sides of Simplified Frigate ONERA (SFO) model. It is found that the blowing jet reduced the re-circulation zone by enhancing mixing activities and entrainment. Moreover, a steady blowing jet is also effective in reducing the unsteadiness in the landing region. With an injection velocity of 2.5% of the free-stream, the unsteadiness was reduced by 6.6%, and such reduction was further improved with high WOD (Shafer and Ghee, 2005). Steady suction flow control was studied on the SFS model by Bardera et al. (2021a). Various suction configurations were tested on

* Corresponding author.
*E-mail addresses:* kewei@chalmers.se (K. Xu), sinisa.krajnovic@chalmers.se (S. Krajnovic).

https://doi.org/10.1016/j.oceaneng.2022.113051
Received 17 March 2022; Received in revised form 3 October 2022; Accepted 28 October 2022
Available online 10 November 2022

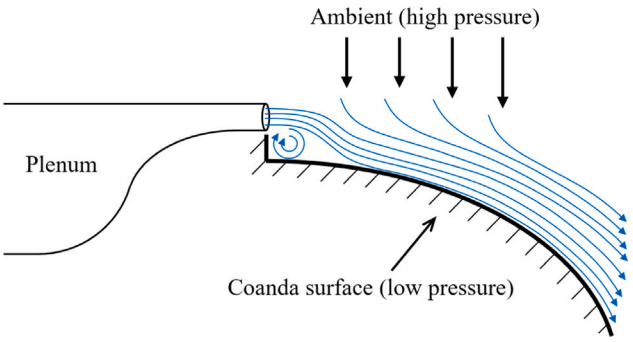


**Fig. 1.** Illustration of the Coanda effect.

the ship deck for the parametric studies of suction holes and suction power. The results suggested that the configuration with the highest flow rate and suction diameter reduced the low-speed zone from 36% to 3%. Matías-García et al. (2019) tested injection and suction on the SFS2 model and found that the injection reduced the low-speed region twice as much as suction.

The previous studies of ship flow control mainly focus on the improvement of helicopter operations, reduction of low-speed area, and suppression of wake unsteadiness. However, minor efforts and attention are paid on reducing the aerodynamic drag of ships. Moreover, the issue regarding energy efficiency is hardly addressed in the previous AFC studies. The question of interest is whether the gain obtained by AFC exceeds the energy consumption of AFC, or in other words if the net benefit can be achieved. Furthermore, the blowing jet used previously is mostly injected tangentially, paralleling with the main flow, which can hardly guide the high-energy main flow towards the re-circulation bubble for energization. Comparatively, a jet vectored by the aforementioned Coanda effect heading towards the bubble would be more efficient to enhance mixing and energy transfer.

This paper aims to reduce the aerodynamic drag of the Chalmers ship model using the steady Coanda effect. The present work combines the experimental study for validating numerical methods and the numerical study using Large Eddy Simulation (LES) for understanding the control mechanism. The Coanda surface and injection slot are implemented at the hanger base near the roof. Two configurations with different injection slot sizes are studied. Except for the comparison of control effectiveness, an analysis of energy efficiency is also conducted to evaluate the net benefit generated by AFC. To authors' knowledge, the Coanda effect with steady-blowing jet has not been studied on ship for aerodynamic drag reduction. The present work is to shed some light on this subject.

The remainder of the paper is organized as follows: Section 2 introduces the experimental setup including wind tunnel facilities, test equipment, and test conditions; It also describes the numerical setup including numerical methods, boundary conditions, and mesh resolutions; Section 3 presents baseline validations as well as flow control results with the discussion of flow control effectiveness, energization mechanism, and energy efficiency.

## 2. Description of work

### 2.1. Experimental setup

The experimental measurements are conducted in the closed-circuit L2 wind tunnel facilities at Chalmers University of Technology (Fig. 2). The closed test section of the wind tunnel has a cross-section of 1.8 m × 1.25 m with a length of 3 m. The speed range of the wind tunnel is 0–60 m/s. The wind tunnel is equipped with balances for force measurements as shown in Fig. 2(a), and advanced pressure measurements.

**Table 1**
Locations of pressure probes ($x/W$).

| Numbers | 1 | 2 | 3 | 4 | 5 | 6 | 7 | 8 | 9 |
|---|---|---|---|---|---|---|---|---|---|
| Locations | 0.08 | 0.14 | 0.24 | 0.54 | 0.73 | 0.92 | 1.10 | 1.25 | 1.38 |

During operation, the air pressure and temperature are measured continuously. The free-stream dynamic pressure and velocity are measured by the pitot tube placed at the beginning of the test section as shown in Fig. 2(c). All the measurements are operated by the lab computer using a fully automated control system, Lab-view software.

The Chalmers ship model (CSM) as shown in Fig. 2(b) is created and used for the present studies. It consists of a bow, hanger, and deck. The width to height ratio (W/h) of the hanger is 0.45, which is similar to that of the simplified ship model (SFS2) (Bardera and Meseguer, 2015). But the width to length ratio (W/L) is significantly increased from 0.1 to 0.25, which widens the room inside the hanger and facilitates the fitting of actuators for active flow control in the future. Details of model dimensions are shown in Fig. 3. The width of 0.26 m is used as the characteristic length for normalization.

The baseline ship model has the hanger base with a square-back shape as shown in Fig. 3 (bottom). The flow control model shown in Fig. 4 is added with an injection slot near the edge between the hanger roof and base, and curves the square-back shape to a quarter-ellipse shape as the Coanda surface. The ellipse has a semi-major axis ($a$) of 20%h and a semi-minor axis ($b$) of 15%h, where h is the hanger height. Curving the square-back to the ellipse shape causes a volume loss of hanger by 0.2%. The present work numerically studies two injection slot sizes, 1%h and 2%h. The shape of the Coanda surface is kept the same in both cases.

The experimental study of the baseline CSM aims to assist the validation of numerical methods. The present work does not include the experimental testing for the flow control cases. The baseline CSM is tested at the free-stream velocity of 5 m/s and the Reynolds number ($Re$) of $8 \times 10^4$ based on the ship width. The drag force and distributions of the pressure coefficients are acquired for the comparison with CFD results. The drag force is measured with a six-component strain-gauge balance from RUAG of type 196-6H that is positioned underneath the tunnel floor as shown in Fig. 2(a). The model is mounted on the balance by a four-holder metal plate and is lifted above the tunnel floor by less than 2 mm to minimize the gap disturbance. The drag force is an averaged value for 20 s. Fig. 5 and Table 1 show the locations of pressure probes (black circles) along the center of deck. The pressure measurements are conducted using the differential pressure scanner 9116 with a scanning frequency of 62.5 Hz and a sampling time of 120 s. The model sits on the floor during the measurement of pressure distribution. The pressure coefficient is obtained by Eq. (1).

$$C_p = \frac{p - p_\infty}{0.5\rho_\infty {U_\infty}^2} \tag{1}$$

where $p$ is measured pressure on deck, $p_\infty$, $\rho_\infty$, and $U_\infty$ are the free-stream pressure, density and velocity.

### 2.2. Numerical setup

The Large Eddy Simulation (LES) is conducted using the commercial finite volume software, Star-CCM+. The governing equations are the incompressible, spatially filtered 3D Navier–Stokes equations, which keep the unsteadiness associated with the large-scale turbulent motion while modeling the small-scale high-frequency components of the fluid motion. The filter width, $\Delta$, is associated with the cell size and is defined as $\Delta = (\Delta_i \Delta_j \Delta_k)^{1/3}$. The Wall-Adapting Local-Eddy Viscosity (WALE) model proposed by Nicoud and Ducros (1999) is employed in the present study to provide the subgrid scale viscosity ($\mu_t$) in the Boussinesq approximation of the subgrid-scale stress tensor. The WALE model has been extensively validated in predicting flows around the

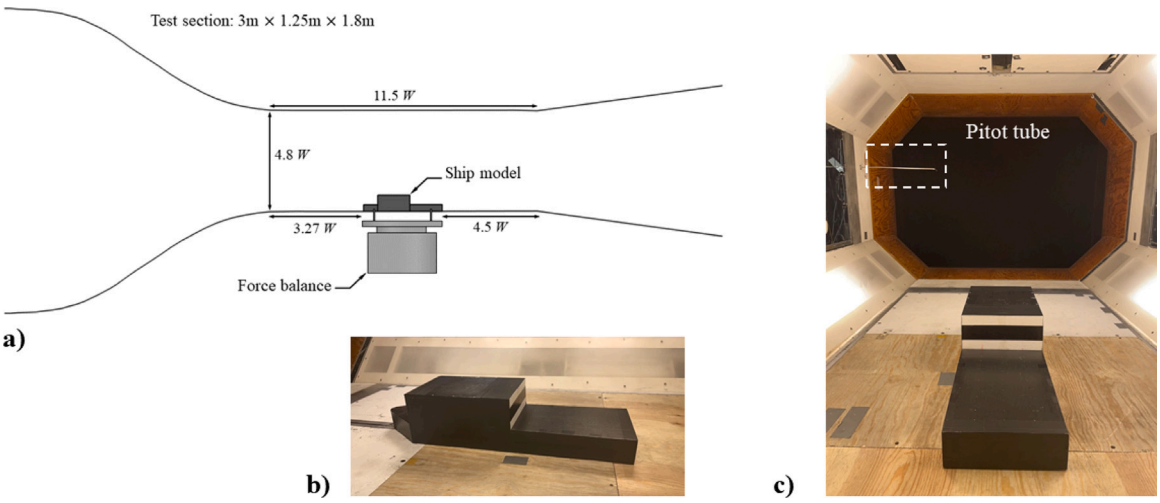


**Fig. 2.** Schematics of Chalmers L2 Wind Tunnel and Chalmers ship model.

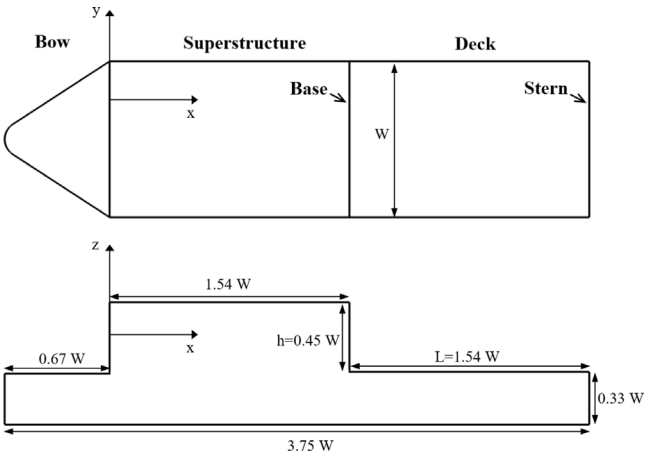


**Fig. 3.** The Chalmers ship dimensions in plan and side views.

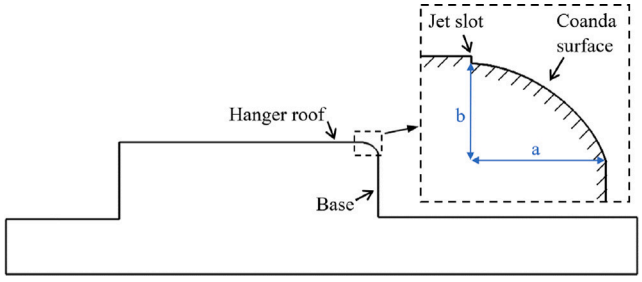


**Fig. 4.** The Chalmers ship dimensions in plan and side views.

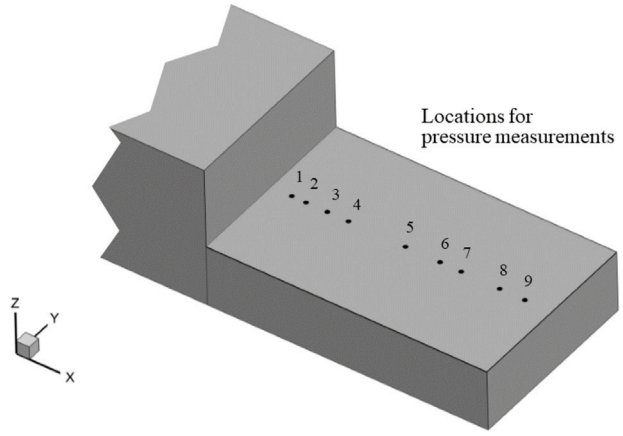


**Fig. 5.** $C_p$ measurement locations at center of deck.

hatchback (Aljure et al., 2014), the squareback (Dalla Longa et al., 2019), and the notchback (He et al., 2021a,b) Ahmed bodies that represent the bluff-body shape of the CSM ship model. The WALE model is, therefore, suitable for the current numerical study.

The WALE model computes the subgrid eddy viscosity based on the invariants of the velocity gradient and accounts for rotational rate. It is defined as

$$\mu_t = \rho(C_w\Delta)^2 \frac{(S^*_{ij}S^*_{ij})^{3/2}}{(\tilde{S}_{ij}\tilde{S}_{ij})^{5/2} + (S^*_{ij}S^*_{ij})^{5/4}} \tag{2}$$

where the model coefficient $C_w$ is 0.544. $\tilde{S}$ is the strain rate tensor that is computed from the resolved velocity field. $S^*_{ij}$ is the traceless symmetric part of the square of the velocity gradient tensor, defined as

$$S^*_{ij} = \frac{1}{2}(\tilde{g}^2_{ij} + \tilde{g}^2_{ji}) - \frac{1}{3}\delta_{ij}\tilde{g}^2_{kk} \tag{3}$$

where $\delta_{ij}$ is the Kronecker delta and $g_{ij} = \partial u_i/\partial x_j$.

The convective flux is evaluated by a bounded central-differencing scheme that blends 98% of the 2nd-order central differencing scheme and 2% of the first-order upwind scheme for robustness purposes. The implicit unsteady solver with 2nd-order Euler implicit scheme is used to approximate the transient term. The physical time step ($\Delta t$) is set to $1.44 \times 10^{-4}$ s, which ensures the CFL (Courant Friedrichs Lewy) number lower than 1 in over 99% cells. The LES simulation starts from the preliminary flow field that is provided by the URANS simulation with $k-\omega$ SST turbulence model. After a characteristic time ($t^* = tU_\infty/h$) of 129 when all the aerodynamic forces become dynamically stable, the LES simulation begins sampling and averaging results for a $t^*$ of 172.

Fig. 6 shows the computational domain with a cross-sectional area of 6.5 W × 5 W, which accounts for a blockage ratio of about 2.4%. The length of the domain is 28 W with 8 W from inlet to bow tip-point and 16 W from stern to outlet. The ship model sits on the floor with no gap in-between. The coordinates system and velocity direction are denoted by $x$ and $u$ in the streamwise direction, $y$ and $v$ in the spanwise direction, and $z$ and $w$ in the vertical direction. The velocity inflow boundary condition with a uniform free-stream velocity $U_\infty$ = 5 m/s

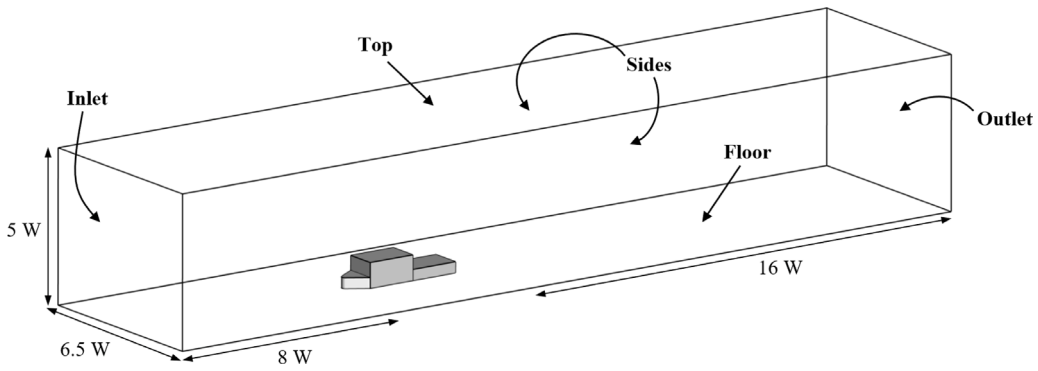


**Fig. 6.** Computational domain.

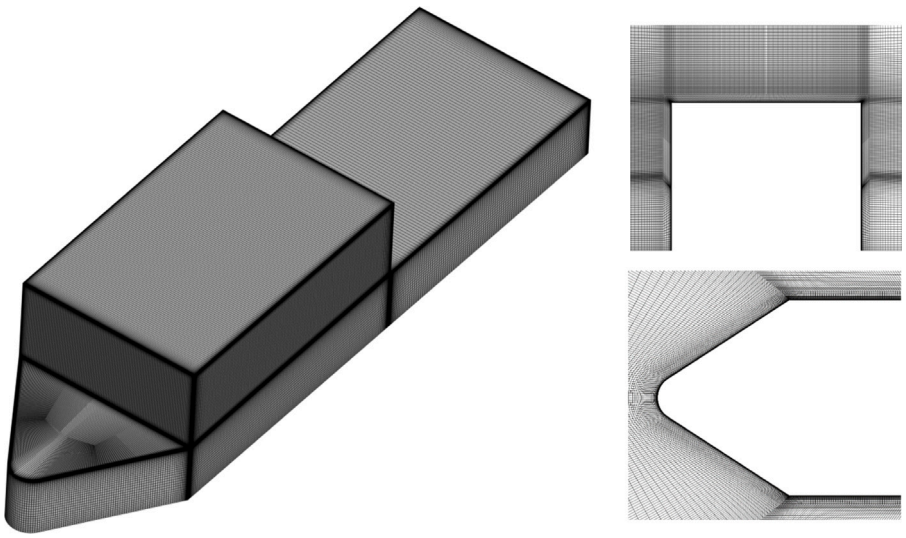

**Fig. 7.** Mesh topology of the Chalmers ship model.

is specified at the inlet. Static pressure outlet boundary condition is applied at the outlet. The top and sides of the domain are specified with symmetry boundary condition. The no-slip wall boundary condition is applied on the floor and all ship surfaces. For the cases with flow control, velocity inlet boundary condition is specified at the injection exit without injection duct simulated.

The structured hexahedral mesh is created using Pointwise. Fig. 7 shows the details of the mesh topology. The overall mesh size contains 37 million cells for the baseline model and 42 million cells for the model with flow control. The near-wall grid distance $\Delta y$ is $3 \times 10^{-5}$, which ensures $y^+ = \frac{\Delta y u_\tau}{\nu}$ lower than 1. For the resolution in streamwise ($\Delta s^+ = \frac{\Delta s u_\tau}{\nu}$) and spanwise ($\Delta l^+ = \frac{\Delta l u_\tau}{\nu}$) directions, the suggested ranges (Piomelli and Chasnov, 1996) are $\Delta s^+ \approx 50 - 150$ and $\Delta l^+ \approx 30 - 50$. For the present case, $\Delta s^+$ is less than 55 and the maximum $\Delta l^+$ is 21. Based on various numerical studies on the ship model with the grid size ranging from 6 to 21 million cells (Zhang et al., 2018; Rao et al., 2019; Zhang et al., 2021), the grid resolution of more than 37 million cells for the present study is sufficient. Therefore, no further grid independent study is conducted.

## 3. Results and discussions

### 3.1. Baseline validation

The numerical method is validated by comparing the drag force and $C_p$ distribution with the experimental measurements. The predicted drag force ($F_D$) is acquired by integrating the surface pressure and wall shear stress in $x$ (free-stream) direction. The drag force is normalized by Eq. (4) to provide the drag coefficient ($C_D$).

$$C_D = \frac{F_D}{0.5\rho_\infty {U_\infty}^2 A_s} \tag{4}$$

where $\rho_\infty$ and $U_\infty$ are the free-stream density and velocity, $A_s$ is the ship cross sectional area.

The predicted $C_D$ is 0.562 and is 4.2% deviated from the experimental value of 0.587.

Then, the $C_p$ distribution along the center of the deck (Fig. 5) is used for further validation. Fig. 8 shows that the predicted and measured $C_p$ distributions are in a good agreement from base ($x/W = 0$) to deck-end ($x/W = 1.54$). The deck pressure first decreases to the minimum due to the re-circulation bubble and then, the flow reattachment on the deck increases pressure to the peak value.

### 3.2. Flow control results

This section presents the results of the controlled ship airflow. There are four cases for comparison labeled as Case 1–4: the baseline ship with square-back hanger, the modified ship with the Coanda surface described in Section 2.1 but no jet blowing, and two flow control cases with the injection slot sizes of 1%h and 2%h. The two flow control cases, Case 3 and 4 are kept with the same blowing velocity of $U_j$ = 5 m/s, which yields the jet momentum coefficients ($C_\mu$) of 0.01 and 0.02 respectively. The momentum coefficient $C_\mu$ is defined as:

$$C_\mu = \frac{\dot{m}_j U_j}{0.5\rho_\infty {U_\infty}^2 A_s} \tag{5}$$

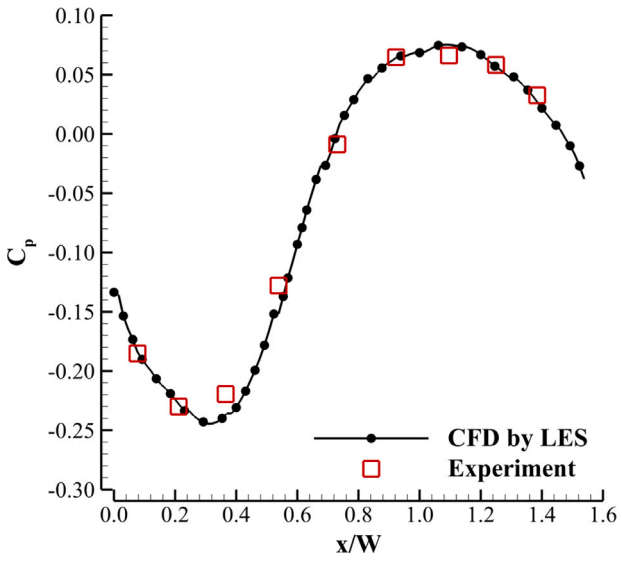


**Fig. 8.** $C_p$ distribution at center of deck.

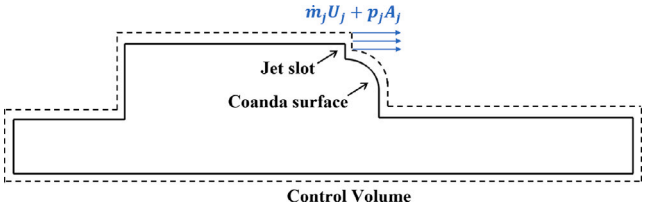


**Fig. 9.** Sketch of control volume analysis.

where $\dot{m}_j$ and $U_j$ are the mass flow rate and velocity of the jet, respectively.

Fig. 9 is a side-view sketch of the ship with flow control applied. The jet slot and Coanda surface are exaggerated for a better demonstration. The control volume (CV) depicted by the dashed line in Fig. 9 encloses the entire ship surface. The drag force is therefore equivalent to the total forces exerted on CV in the $x$ direction, which includes the integration of pressure as well as shear stress, and jet reaction force. The drag force can be expressed by Eq. (6).

$$F_D = \oint_{CV} (p + \tau_w) \cdot \vec{n}\, dA + (\dot{m}_j U_j + p_j A_j) = F_{Dp} + F_{Dj} \tag{6}$$

where $\tau_w$ is the wall shear stress, $\vec{n}$ is the unit vector in $x$ direction, $A$ is the area of the control volume, $p_j$ is the pressure at the jet exit and $A_j$ is the area of the jet slot. Eq. (6) consists of two terms, the surface-integration term $F_{Dp}$ and jet-reaction term $F_{Dj}$. Obviously, the reduction of $F_D$ can be attributed to the reduction of $F_{Dp}$ and of $F_{Dj}$. In the present study, the reduction of $F_{Dp}$ correlates with the pressure recovery of the ship base. The reduction of $F_{Dj}$ can be achieved by applying a stronger jet, which requires a higher $C_\mu$ and increases energy consumption. Therefore, from the energy efficient point of view, it is expected to have the reduction of $F_{Dp}$ dominates the overall drag reduction.

Following Eq. (4), we also have the drag coefficients $C_{Dp}$ and $C_{Dj}$ for $F_{Dp}$ and $F_{Dj}$ respectively. Table 2 compares the drag coefficients of the four cases with their breakdowns of $C_{Dp}$ and $C_{Dj}$. Case 2 increases the ship drag slightly, which indicates that only modifying the hanger shape with the Coanda surface does not contribute to the drag reduction. A reduction of 5.34% is achieved by Case 3 and is even higher in Case 4 of 6.22%. However, most of the drag reduction in Case 4 comes from the term $C_{Dj}$ due to the doubled $C_\mu$, and term $C_{Dp}$ is actually increased compared to Case 3. This suggests that Case 4 has less control effectiveness with lower pressure recovery, and its drag reduction will require higher energy consumption. Note that the drag reduction of 5.34% and 6.22% may sound small, but is much more significant compared to the drag reduction of less than 2% achieved by the base cavity flow control applied on the SFS2 ship model in Rao et al. (2019).

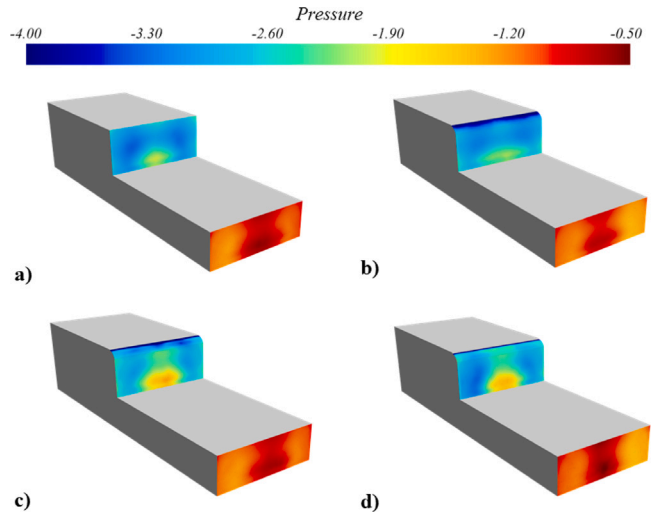


**Fig. 10.** Time-averaged pressure contours at base and stern: (a) Case 1, (b) Case 2, (c) Case 3, (d) Case 4.

**Table 2**
Drag forces comparison among Case 1–4.

| Cases | $C_D$ | $\Delta C_D$ | $C_{Dp}$ | $C_{Dj}$ | $C_\mu$ |
|---|---|---|---|---|---|
| 1 | 0.562 | – | 0.562 | – | – |
| 2 | 0.565 | −0.53% | 0.565 | – | – |
| 3 | 0.532 | 5.34% | 0.542 | −0.01 | 0.01 |
| 4 | 0.527 | 6.22% | 0.547 | −0.02 | 0.02 |

Fig. 10 shows the time-averaged static pressure contours at the hanger base and stern of the four cases. Gauge pressure is used here with a unit of [Pa]. It is observed that all cases have lower pressure near the sides of the base and high value at the center-bottom location. With the shape modification, Case 2 achieves a minor pressure recovery at the center-bottom location but further reduced pressure at sides as well as on the Coanda surface (top of the base). Comparatively, a significant pressure increase is observed all over the base in Case 3. Case 4 is observed with a lower base pressure recovery than Case 3. The area-averaged base pressure coefficient of Case 3 is increased by 14.0% compared to the baseline case. Such pressure recovery is 44.3% higher than that achieved by Case 4, which explains the $C_{Dp}$ difference in Table 2. The stern pressure is distributed similarly among the four cases with the pressure coefficients of the baseline case slightly higher than those of Case 3 and 4 by less than 4%. Such a small pressure coefficient variation has an even minor effect on drag because the stern section contributes marginally to the overall drag.

Fig. 11 shows the time-averaged streamwise velocity ($u$) contours on the ship's symmetric plane. A low-speed area (LSA) is observed downstream the hanger base, which is quantified using the area enclosed by the iso-line of $u = 0$. The LSA of the four cases is extracted and overlapped in Fig. 12. The area of LSA in each case is normalized by the total area above the deck $hL$ (enclosed by the dash–dot line in Fig. 11(a)), where the $h$ is the hanger height and $L$ is the deck length (Bardera et al., 2021b). Case 1 has the largest LSA of 0.34 and is substantially reduced by 32.3% in Case 2. Case 3 has a little higher size of LSA than Case 2, whereas Case 4 with a larger $C_\mu$ achieves an increased LSA by 16.0% compared to Case 3. Moreover, comparing to Case 1, the reattachment length is reduced by 15.4% in Case 2,

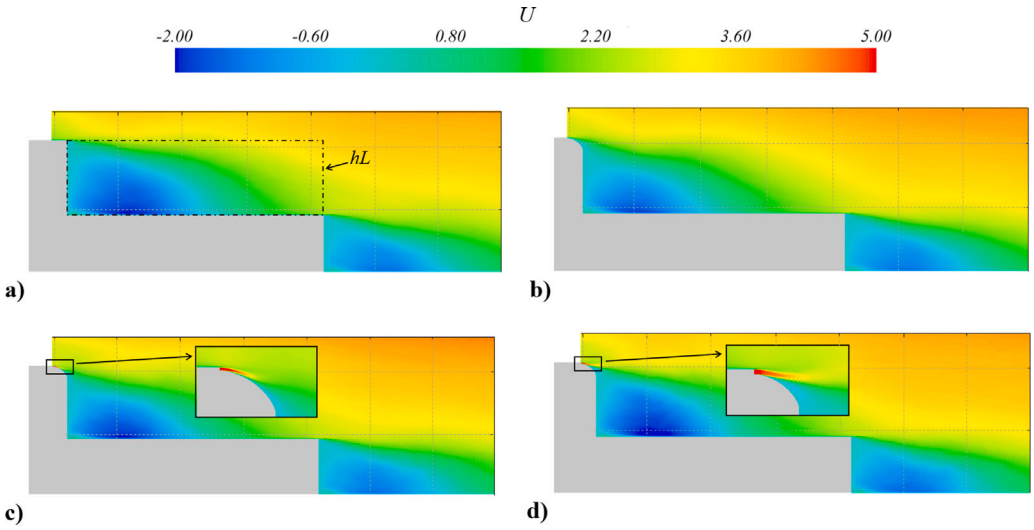


**Fig. 11.** Time-averaged $u$ velocity contours at the symmetric plane: (a) Case 1, (b) Case 2, (c) Case 3, (d) Case 4.

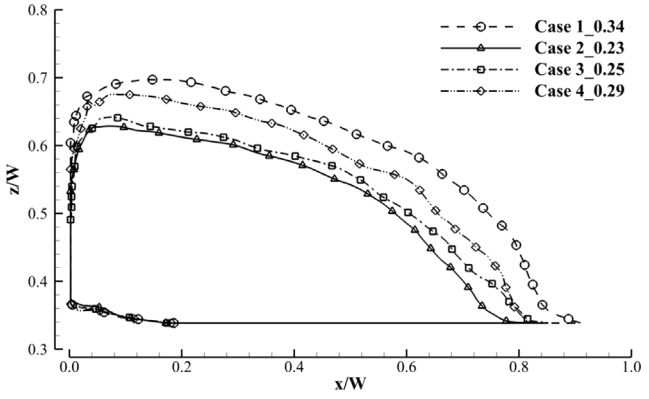


**Fig. 12.** Iso-line with $u = 0$ in the symmetric plane.

and Cases 3 and 4 have the similar but lower reduction of length of 11.0%. The suppression of LSA and earlier attachment of the separation bubble optimize the flow condition on the deck, which will improve the landing environment and pilot safety.

As shown in the zoomed-in view of Fig. 11(c) and (d), Case 4 with a wider slot size has the jet flow detached earlier from the Coanda surface, which is ineffective to suppress LSA. A question of interest is why does a wider slot size lead to an earlier detachment of jet? As reviewed in Section 1, jet flow attaches on the Coanda surface due to flow entrainment that reduces the surface pressure and enhances the pressure gradient for attachment. With the jet velocity kept the same in Case 3 and 4, the entrainment effects are similar. But the wider slot size in Case 4 increases the momentum of the jet in the direction that deviates from the Coanda surface. Consequently, the pressure gradient induced by Coanda effect is no longer sufficient to attach the jet.

Case 2 in Fig. 12 achieves an even smaller LSA than Case 3, suggesting that the Coanda surface is effective to suppress LSA without jet blowing. However, such suppressed LSA in Case 2 does not generate much pressure recovery as shown in Fig. 10(b). This can be explained by Fig. 13 that compares the time-averaged total pressure and static pressure distribution at the symmetric plane of Case 2 and 3. As shown in Fig. 13(a) and (b), Case 3 has the low total pressure zone significantly inhibited due to the energization from the jet flow. The flow downstream the base in Case 3 is therefore at the high-energy state that increases the static pressure near the base as compared in Fig. 13(c) and (d). The low-static-pressure zone appears to be pushed away from the base, and the pressure recovery is therefore achieved in Case 3.

To further demonstrate the energization process and control mechanism of the steady Coanda effects, Fig. 14 shows the time-averaged $y$-vorticity (spanwise) contours at the ship symmetric plane. Strong vorticity sheets are observed downstream the ship hanger and stern. It can be observed that Case 4 has the strongest vorticity, however, it does not achieve the best pressure recovery as shown in Fig. 10. This can be explained by the vorticity vectoring effects. To facilitate demonstration, $\alpha$ is defined as the angle of the vorticity sheet downstream the base to horizontal and $\beta$ denotes the one downstream stern. The higher the angle, the more penetration of the vorticity into LSA, meaning that the energy transfer occurs at where it is more needed. As shown in Fig. 14, angle $\alpha$ is 11° in Case 1 and is increased to 15° in Case 2. The highest $\alpha$ is achieved in Case 3 with 24° due to the induction effect from the well-attached jet. Case 4 has $\alpha$ reduced to 16° because of the earlier detachment of jet. The 3D iso-surface with y-vorticity = 70 is shown in Fig. 15, where the orange line highlights the vectoring of vorticity sheets. Case 3 has vorticity more vectored towards the deck, meaning the LSA on deck is strongly influenced. Although Case 4 increases the intensity of vorticity with a higher $C_\mu$, the high vorticity zone locates away from the LSA, which is ineffective for energization. For the vectoring angle $\beta$ of the vorticity downstream the stern, the four cases are close with one another, ranging from 11° to 14°. This indicates that the energization process for the stern re-circulation bubble is quite similar, which is the reason for stern pressure not varying notably among baseline and controlled cases as shown in Fig. 10.

Fig. 16 shows the turbulent kinetic energy (TKE) contours downstream the hanger base. TKE is defined as $0.5(\overline{u'u'} + \overline{v'v'} + \overline{w'w'})$, representing energy dissipation. Without jet blowing, Case 1 and 2 have TKE sparsely distributed with a low maximum value of 1.51 and 1.52 respectively. With the blowing jet, a condensed high TKE zone is observed in Case 3 with a maximum of 1.66 and is further increased to 1.78 in Case 4, which suggests an enhanced mixing process. The positions of the high-TKE zone in Case 3 and 4 are indicated using Point C which approaches the center of the high-TKE zone. Compared with Case 3, Case 4 has the point C shifted upwards from the deck by 10.1%, meaning the LSA is less influenced by an ineffective mixing process. Therefore, although Case 4 has a larger high-TKE zone with higher maximal TKE, it still achieves a lower pressure recovery. This also agrees with the previous observations illustrated by vorticity vectoring in Figs. 14 and 15.

Moreover, TKE also indicates the intensity of turbulent activity, and the airwake with a suppressed turbulent activity on the deck

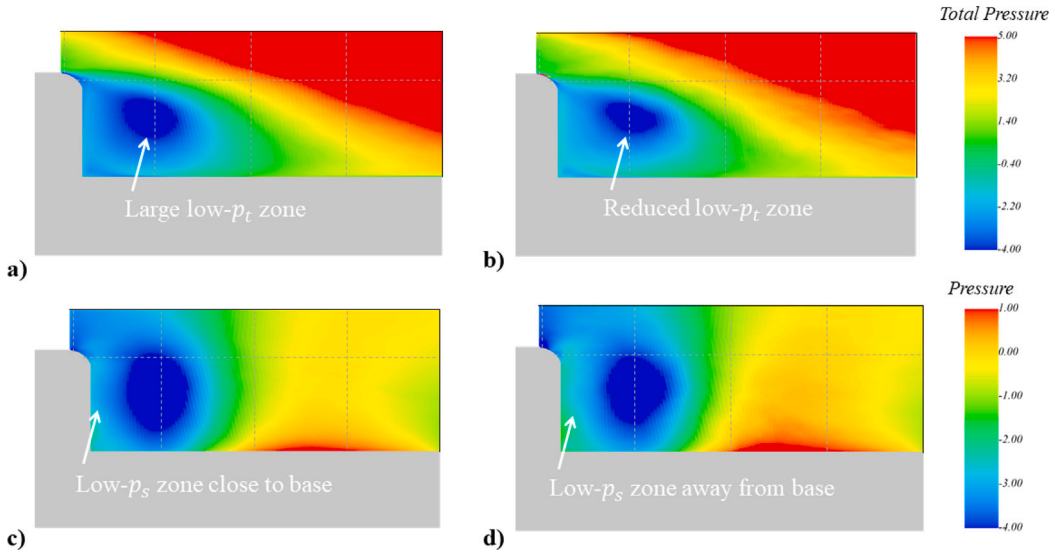


**Fig. 13.** Time-averaged total ($p_t$) and static ($p_s$) pressure contours at the symmetric plane: (a) Case 2 $p_t$, (b) Case 3 $p_t$, (c) Case 2 $p_s$, (d) Case 3 $p_s$.

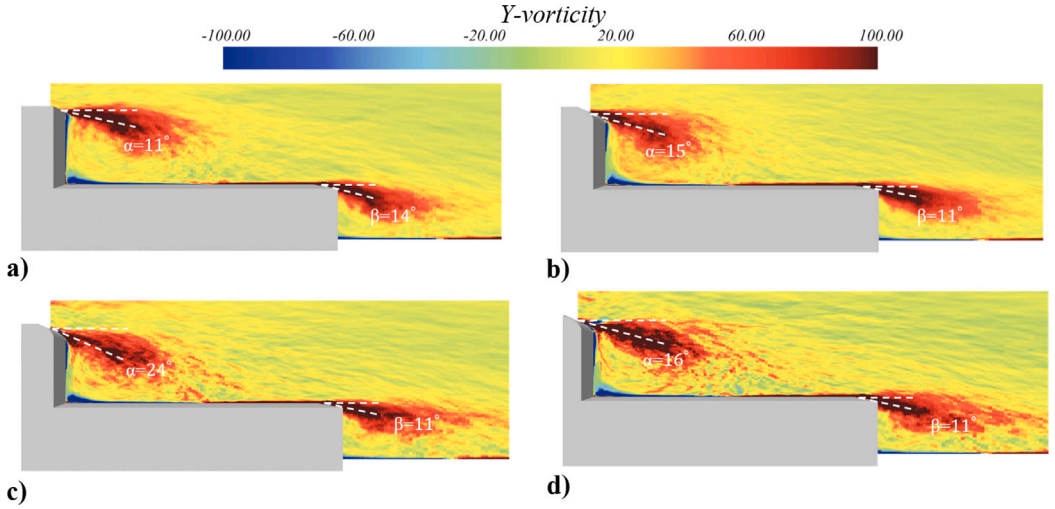


**Fig. 14.** Time-averaged $y$ vorticity contours at the symmetric plane: (a) Case 1, (b) Case, 2 (c) Case 3, (d) Case 4.

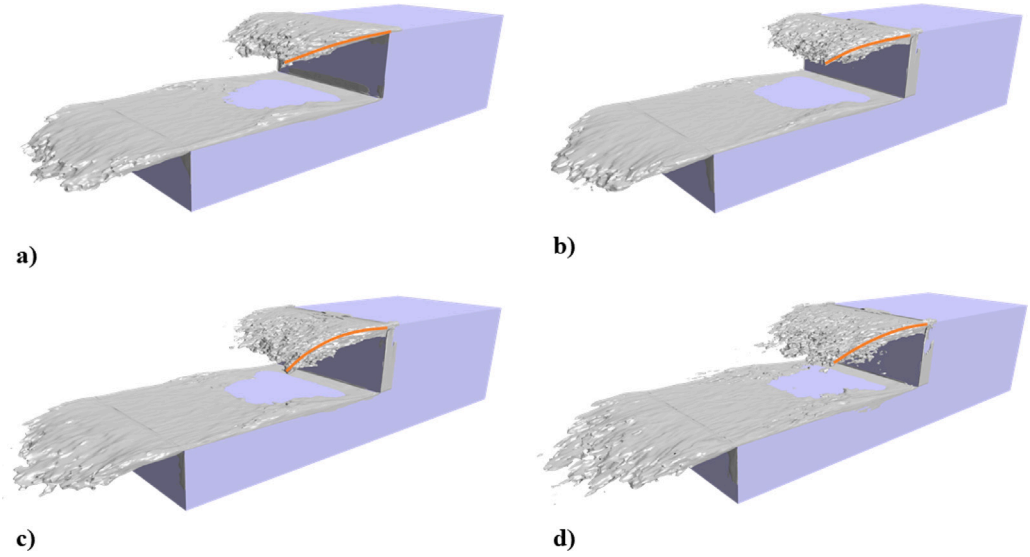


**Fig. 15.** Iso-surface of $y$-vorticity with $\omega_y$ = 70: (a) Case 1, (b) Case 2, (c) Case 3, (d) Case 4.

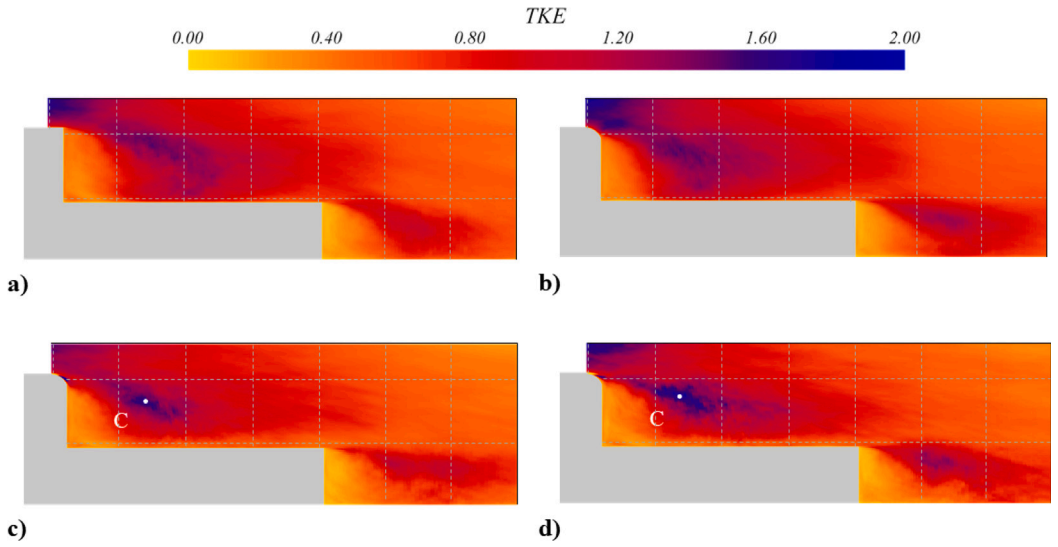


**Fig. 16.** Turbulent kinetic energy contours at the symmetric plane: (a) Case 1, (b) Case 2, (c) Case 3, (d) Case 4.

significantly reduces the pilot workload (Bardera and Meseguer, 2015). Among the four cases in Fig. 16, the size of the high-TKE region in Case 3 is the minimal, which is mostly dissipated within the first two grids measured from the base (marked by the gray-dashed line). This is because the vectored jet flow with the $C_\mu$ of 0.01 enhances the turbulent mixing and guides it towards the base and deck. The high-TKE region with the mitigated size and length is more likely to avoid intercepting the helicopter path, which reduces the perceived pilot workload (Gallas et al., 2017).

### 3.3. Analysis of energy efficiency

Effectiveness and efficiency are the two crucial aspects to evaluate an active flow control method. Effectiveness means the control authority, in the present case, the drag reduction. Efficiency indicates the energy consumption of the AFC. It determines if the flow control method is affordable or cost-effective.

To demonstrate the energy efficiency of the present flow control, the following parameters are defined. The power saving ($P_s$) for the ship due to drag reduction ($\Delta F_D$) is defined by Eq. (7).

$$P_s = \Delta F_D U_\infty \tag{7}$$

Eq. (6) indicates that the overall drag $F_D$ can be decomposed to the surface-integration term $F_{Dp}$ and the jet-reaction term $F_{Dj}$. Similarly, the reduction of the overall drag $\Delta F_D$ and overall power saving $P_s$ can be also decomposed following the same rule in Eq. (6). Therefore, Eq. (7) becomes

$$P_s = (\Delta F_{Dp} + \Delta F_{Dj})U_\infty = P_{sp} + P_{sj} \tag{8}$$

where $P_{sp}$ and $P_{sj}$ represent the power saving from the reduction of surface-integration term ($\Delta F_{Dp}$) and jet-reaction force ($\Delta F_{Dj}$) respectively.

$P_s$ can be normalized to the non-dimensional power saving coefficient $\overline{P_s}$ by Eq. (9). Similarly, we also have $\overline{P_{sp}}$ and $\overline{P_{sj}}$.

$$\overline{P_s} = \frac{P_s}{0.5\rho_\infty {U_\infty}^3 A_s} \tag{9}$$

$\overline{P_s}$ represents the overall energy saving without considering the power consumed by AFC. For the power required (PR) by AFC, the power coefficient $P_c$ is suggested as an appropriate metric in Xu et al. (2022), which is based on the total enthalpy change ($\Delta H_t$) of the AFC actuator. However, the obtainment of $\Delta H_t$ requires the AFC to be zero-net-mass-flux (ZNMF) or in other words, a closed system with injection (source) and suction (sink). The steady blowing jet used herein is an open system with non-zero-net-mass-flux (non-ZNMF), which lacks of suction, and therefore $\Delta H_t$ can be hardly acquired. In this case, the energy evaluation is conducted following the practice by Seifert et al. (1998) and Borgmann et al. (2017) who use the energy coefficient ($C_E$) to quantify the power consumption of the non-ZNMF sweeping jet actuators (Graff et al., 2013). $C_E$ estimates the kinetic energy of the jet with the assumption that the injection duct has the static pressure of the jet flow losslessly converted to the dynamic pressure (Borgmann et al., 2017). The present case meets such a condition because a velocity inlet boundary condition is directly specified at the exit of the injection duct and the duct flow simulation is avoided. $C_E$ is defined

$$C_E = \frac{P}{0.5\rho_\infty {U_\infty}^3 A_s} = \frac{(0.5\rho_j {U_j}^2 A_j)U_j}{0.5\rho_\infty {U_\infty}^3 A_s} = \frac{C_\mu}{2}\frac{U_j}{U_\infty} \tag{10}$$

where $\rho_j$ is the density of the jet flow.

The non-dimensional net power saving coefficient ($\overline{\Delta P_s}$) is defined $\overline{\Delta P_s} = \overline{P_s} - C_E$, which represents the power saving subtracting the power spent by AFC. The energy efficiency ($\eta$) is the ratio of the net power saving coefficient $\overline{\Delta P_s}$ to the overall power saving $\overline{P_s}$ of AFC, $\eta = \overline{\Delta P_s}/\overline{P_s}$. If $\eta > 0$, the net benefit is achieved. The higher the $\eta$ (closer to 100%), the more cost-effective the AFC is.

**Table 3**
Energy efficiency comparison of Case 3 and Case 4.

| Cases | $C_\mu$ | $\overline{P_s}$ | $\overline{P_{sp}}$ | $\overline{P_{sj}}$ | $C_E$ | $\overline{\Delta P_s}$ | $\eta$ |
|---|---|---|---|---|---|---|---|
| 3 | 0.01 | 0.03 | 0.02 | 0.01 | 0.005 | 0.025 | 83.3% |
| 4 | 0.02 | 0.035 | 0.015 | 0.02 | 0.01 | 0.025 | 71.4% |

As shown in Table 3, Cases 3 and 4 have the energy efficiency $\eta$ higher than 0, meaning that the net benefit is achieved in both cases. Although $\overline{P_s}$ in Case 3 is 14.2% lower than Case 4, the energy coefficient $C_E$ is halved, which yields a 11.9% higher energy efficiency $\eta$. Case 4 has the majority of its $\overline{P_s}$ from jet-reaction term $\overline{P_{sj}}$ and hence, reduces $\eta$. Note that $\overline{\Delta P_s}$ of Case 3 and 4 are the same, however, they are resulted from a significantly different energy consumption as indicated by $C_E$. Case 3 with a more pronounced Coanda effect achieves 33.3% higher $\overline{P_{sp}}$ than Case 4 and is therefore more efficient.

## 4. Conclusions

The present work studies the steady Coanda effect for reducing the aerodynamic drag of the Chalmers ship model (CSM). Modifications are

made at the hanger base with the addition of the Coanda surface and jet-blowing slot. Four cases are studied: the baseline CSM, modified CSM without jet, and two jet-blowing cases with different slot sizes. The Large Eddy Simulation (LES) with the Wall-Adapting Local-Eddy Viscosity (WALE) model is conducted for understanding the control mechanism. The baseline CSM is experimentally tested to provide data for numerical validations.

Only with the shape modification of the Coanda surface, the ship drag is sightly increased but the low-speed area on deck is significantly suppressed. Together with jet blowing, a drag reduction of 5.34% is achieved in the small slot-size case with a base pressure recovery of 14%. A higher drag reduction of 6.22% is achieved in the large slot-size case due to the doubled jet momentum coefficient, however, it comes with higher power consumption and lower energy efficiency. It is found that vectoring vorticity towards the low-speed area on deck is more effective for enhancing energization and mixing process than merely increasing the intensity of vorticity. Moreover, the turbulent kinetic energy (TKE) contours suggest that the steady Coanda effect also reduces the size and length of the high-TKE region on deck, which benefits the maneuvers of aircraft.

The energy efficiency of the present flow control is analyzed by comparing the overall and net power saving coefficients of AFC, $\overline{P_s}$ and $\overline{\Delta P_s}$. The net benefit is achieved in both the cases with flow control, and the case with the small slot size has higher energy efficiency due to a stronger Coanda effect.

The aerodynamic drag may be small compared to water resistance but is still counted in the power prediction of ship propulsion, contributing to about 10% of the overall power consumption. If a 10% reduction of aerodynamic drag can be achieved with further optimization of flow control, the power consumption can be reduced by 1%, which is worth the effort.

Nowadays, aerodynamic drag is not sufficiently considered during ship design, and so is the reduction of aerodynamic drag. However, when it comes to the future fully-electric fossil-fuel-free ships, all contributions to drag reduction matter. The current study demonstrates the potential of such contribution from an active flow control perspective.

## CRediT authorship contribution statement

**Kewei Xu:** Conceptualization, Methodology, Software, Validation, Formal analysis, Investigation, Data curation, Writing – original draft, Writing – review & editing, Visualization. **Xinchao Su:** Software, Investigation, Validation. **Rickard Bensow:** Validation, Writing – review & editing, Supervision, Project administration, Funding acquisition. **Sinisa Krajnovic:** Resources, Validation, Writing – review & editing, Supervision, Project administration, Funding acquisition.

## Declaration of competing interest

The authors declare that they have no known competing financial interests or personal relationships that could have appeared to influence the work reported in this paper.

## Data availability

Data will be made available on request.

## Acknowledgments

This work is supported by the Chalmers University of Technology, Sweden. The authors would like to acknowledge the computing resource provided by SNIC (Swedish National Infrastructure for Computing) at the National Supercomputer Center (NSC) at Linköping University. The authors also thank Prof. Jie Zhang at Central South University for his effort on the ship model design.

## References

Aljure, D.E., Lehmkuhl, O., Rodriguez, I., Oliva, A., 2014. Flow and turbulent structures around simplified car models. Comput. & Fluids 96, 122–135.
Bardera, R., Matías, J.C., Barroso, E., 2021a. Experimental and numerical simulations of simple frigate with suction flow control over the deck. Ocean Eng. 236, 109464.
Bardera, M.R., Matías García, J.C., García-Magariño, A., 2021b. Aerodynamic optimization over frigate helicopter flight deck by hangar shape modifications. AIAA J. 59, 1387–1397.
Bardera, R., Meseguer, J., 2015. Flow in the near air wake of a modified frigate. Proc. Inst. Mech. Eng. G 229, 1003–1012.
Barros, D., Borée, J., Noack, B.R., Spohn, A., Ruiz, T., 2016. Bluff body drag manipulation using pulsed jets and Coanda effect. J. Fluid Mech. 805, 422–459.
Borgmann, D., Pande, A., Little, J.C., Woszidlo, R., 2017. Experimental study of discrete jet forcing for flow separation control on a wall mounted hump. In: 55th AIAA Aerospace Sciences Meeting. p. 1450.
Crozon, C., Steijl, R., Barakos, G.N., 2018. Coupled flight dynamics and CFD–demonstration for helicopters in shipborne environment. Aeronaut. J. 122, 42–82.
Dalla Longa, L., Evstafyeva, O., Morgans, A.S., 2019. Simulations of the bi-modal wake past three-dimensional blunt bluff bodies. J. Fluid Mech. 866, 791–809.
Forrest, J.S., Owen, I., 2010. An investigation of ship airwakes using Detached-Eddy Simulation. Comput. & Fluids 39, 656–673.
Freund, J.B., Mungal, M.G., 1994. Drag and wake modification of axisymmetric bluff bodies using Coanda blowing. J. Aircr. 31, 572–578.
Gallas, Q., Lamoureux, M., Monnier, J.-C., Gilliot, A., Verbeke, C., Delva, J., 2017. Experimental flow control on a simplified ship helideck. AIAA J. 55, 3356–3370.
Geropp, D., Odenthal, H.-J., 2000. Drag reduction of motor vehicles by active flow control using the Coanda effect. Exp. Fluids 28, 74–85.
Graff, E., Seele, R., Lin, J.C., Wygnanski, I., 2013. Sweeping Jet Actuators-a New Design Tool for High Lift Generation. Technical Report.
Haffner, Y., Borée, J., Spohn, A., Castelain, T., 2020. Unsteady coanda effect and drag reduction for a turbulent wake. J. Fluid Mech. 899.
He, K., Minelli, G., Wang, J., Dong, T., Gao, G., Krajnović, S., 2021a. Numerical investigation of the wake bi-stability behind a notchback Ahmed body. J. Fluid Mech. 926.
He, K., Minelli, G., Wang, J., Gao, G., Krajnović, S., 2021b. Assessment of LES, IDDES and RANS approaches for prediction of wakes behind notchback road vehicles. J. Wind Eng. Ind. Aerodyn. 217, 104737.
Herry, B.B., Keirsbulck, L., Labraga, L., Paquet, J.-B., 2011. Flow bistability downstream of three-dimensional double backward facing steps at zero-degree sideslip. J. Fluids Eng. 133.
Jones, G.S., 2005. Pneumatic flap performance for a 2D circulation control airfoil, stedy & pulsed. In: Applications of Circulation Control Technologies. pp. 191–244.
Jones, G., Viken, S., Washburn, A., Jenkins, L., Cagle, C., 2002. An active flow circulation controlled flap concept for general aviation aircraft applications. In: 1st Flow Control Conference. p. 3157.
Kääriä, C.H., Wang, Y., White, M.D., Owen, I., 2013. An experimental technique for evaluating the aerodynamic impact of ship superstructures on helicopter operations. Ocean Eng. 61, 97–108.
Kee, J.-D., Kim, M.-S., Lee, B.-C., 2001. The COANDA flow control and Newtonian concept approach to achieve drag reduction of passenger vehicle. SAE Trans. 1383–1400.
Matías-García, J., Franchini-Longhi, S., Bardera, R., 2019. Vortex generators and active flow control in the aft-deck of a frigate. In: 8th European Conference for Aeronautics and Space Sciences, Madrid, Spain. pp. 1–4.
Nicoud, F., Ducros, F., 1999. Subgrid-scale stress modelling based on the square of the velocity gradient tensor. Flow Turbul. Combust. 62, 183–200.
Piomelli, U., Chasnov, J.R., 1996. Large-eddy simulations: Theory and applications. In: Turbulence and Transition Modelling. Springer, pp. 269–336.
Rao, A.N., Zhang, J., Minelli, G., Basara, B., Krajnović, S., 2019. Qualitative assessment of the bi-stable states in the wake of a finite-width double backward facing step. J. Wind Eng. Ind. Aerodyn. 186, 241–249.
Seele, R., Graff, E., Lin, J., Wygnanski, I., 2013. Performance enhancement of a vertical tail model with sweeping jet actuators. In: 51st AIAA Aerospace Sciences Meeting Including the New Horizons Forum and Aerospace Exposition. p. 411.
Seifert, A., Eliahu, S., Greenblatt, D., Wygnanski, I., 1998. Use of piezoelectric actuators for airfoil separation control. AIAA J. 36, 1535–1537.
Sellars, N., Wood, N., Kennaugh, A., 2002. Delta wing circulation control using the coanda effect. In: 1st Flow Control Conference. p. 3269.
Shafer, D., Ghee, T., 2005. Active and passive flow control over the flight deck of small naval vessels. In: 35th AIAA Fluid Dynamics Conference and Exhibit. p. 5265.
Syms, G.F., 2008. Simulation of simplified-frigate airwakes using a lattice-Boltzmann method. J. Wind Eng. Ind. Aerodyn. 96, 1197–1206.
Tritton, D.J., 2012. Physical Fluid Dynamics. Springer Science & Business Media.
Xu, K., Ren, Y., Zha, G., 2022. Numerical analysis of energy expenditure for coflow wall jet separation control. AIAA J. 1–19.
Zhang, J., Minelli, G., Basara, B., Bensow, R., Krajnović, S., 2021. Yaw effect on bi-stable air-wakes of a generic ship using large eddy simulation. Ocean Eng. 219, 108164.
Zhang, J., Minelli, G., Rao, A.N., Basara, B., Bensow, R., Krajnović, S., 2018. Comparison of PANS and LES of the flow past a generic ship. Ocean Eng. 165, 221–236.